



A Mg²⁺/polydopamine composite hydrogel for the acceleration of infected wound healing

Zhaoyuan Guo^{a,b}, Zhuangzhuang Zhang^b, Nan Zhang^b, Wenxia Gao^{a,*}, Jing Li^b, Yuji Pu^b, Bin He^{b,**}, Jing Xie^{c,***}

^a College of Chemistry and Materials Engineering, Wenzhou University, Wenzhou, 325035, China

^b National Engineering Research Center for Biomaterials, College of Biomedical Engineering, Sichuan University, Chengdu, 610065, China

^c Department of Stomatology, The First Affiliated Hospital of Wenzhou Medical University, Wenzhou, 325000, China

ARTICLE INFO

Keywords:

Multifunctional hydrogel
Self-healing
Tissue adhesiveness
Photothermal antibacterial effect
Wound healing

ABSTRACT

Bacterial infection is a vital factor to delay the wound healing process. The antibiotics abuse leads to drug resistance of some pathogenic bacteria. Non-antibiotic-dependent multifunctional biomaterials with accelerated wound healing performance are urgently desired. Herein, we reported a composite antibacterial hydrogel PDA-PAM/Mg²⁺ that shows excellent self-healing and tissue adhesive property, and photothermal antibacterial functions for accelerating wound healing. The gel was composed of polyacrylamide (PAM), polydopamine (PDA), and magnesium (Mg²⁺) and prepared via a two-step procedure: an alkali-induced dopamine pre-polymerization and followed radical polymerization process. The composite gel shows excellent tissue adhesiveness and Mg²⁺-synergized photothermal antibacterial activity, inducing a survival rate of 5.29% for *S. aureus* and 7.06% for *E. coli* after near infrared light irradiation. The composite hydrogel further demonstrated efficient bacteria inhibition, enhanced wound healing and collagen deposition in a full-thickness skin defect rat model. Together, the PDA-PAM/Mg²⁺ hydrogel presents an excellent wound dressing with excellent tissue adhesion, wound healing, and antibacterial functions.

1. Introduction

Skin is the largest organ of human and functions as a protective barrier [1]. Damaged skin loses the barrier function, which makes it susceptible to wound infections that aggravate the skin injury and even causes death [2,3]. Biomaterials have been used to avoid infections during wound healing. However, the traditional treatments, such as inorganic antimicrobials, would cause severe systemic toxicity to result in antibiotics resistance [4]. Therefore, new strategies are needed to accelerate wound healing.

Photothermal therapy (PTT) that leverages photothermal reagents to convert laser light energy into thermal energy has emerged as a new strategy with great potential for antibacterial activity. It physically eliminates microorganisms via a variety of hyperthermia effects, including protein/enzyme denaturation, cell membrane rupture, cell cavitation, and cell fluid evaporation [5,6]. Furthermore, as a

antimicrobial tool, it exhibits many advantages: targeting selectivity, deep tissue/biofilm penetration, remote controllability, non-invasiveness, rapid effectiveness, and fewer side effects [7]. In recent years, many nanomaterials have been developed for photothermal antibacterial therapy [8–11]. For example, Ma et al. [12] constructed core-shell nanomaterials (GNR@LDH-PEG) of gold nanorods (GNRs) and layered double hydroxides (LDHs), which fulfilled a 99.25% inhibition of *Escherichia coli* (*E. coli*) and 88.44% for *Staphylococcus aureus* (*S. aureus*) upon treatment with a 5-min near infrared (NIR) irradiation. Deng et al. [13] designed dual-valent platinum nanoparticles (dvPtNPs) that are composed of a Pt⁰ core and a Pt²⁺ shell. Under NIR irradiation, dvPtNPs efficiently killed *E. coli* and methicillin-resistant *Staphylococcus aureus* (MRSA) both *in vitro* and *in vivo*. Noteworthy, when the photothermal nanomaterials are directly applied on the wound surfaces, excessive topical concentrations and cytotoxicity are unavoidable [14]. To this end, a stable medium is

Peer review under responsibility of KeAi Communications Co., Ltd.

* Corresponding author.

** Corresponding author.

*** Corresponding author.

E-mail addresses: wenxiag@wzu.edu.cn (W. Gao), bhe@scu.edu.cn (B. He), xiejing@wmu.edu.cn (J. Xie).

<https://doi.org/10.1016/j.bioactmat.2021.11.036>

Received 14 September 2021; Received in revised form 15 November 2021; Accepted 27 November 2021

Available online 20 December 2021

2452-199X/© 2021 The Authors. Publishing services by Elsevier B.V. on behalf of KeAi Communications Co. Ltd. This is an open access article under the CC BY-NC-ND license (<http://creativecommons.org/licenses/by-nc-nd/4.0/>).

needed to uniformly disperse the photothermal agents and maintain the antibacterial effects for a longer time.

Hydrogels are soft materials with three-dimensional network structures and are ideal multifunctional wound dressings with merits of maintaining the moist microenvironment, allowing water and oxygen permeation, absorbing excess exudates, and shielding microorganisms [15,16]. These functions are fundamental and important for wound healing via promoting fibroblast proliferation, keratinocyte migration, and eventual re-epithelialization [17–20]. However, the weak mechanical properties and lack of adhesiveness result in impaired performance of most hydrogels [21]. Therefore, multi-functional hydrogels with tunable chemical and mechanical properties are expected to address the limitations of currently available alternatives [22,23].

In this study, a photothermal PDA-PAM/Mg²⁺ composite hydrogel with self-healing and adhesiveness was designed. As shown in Fig. 1, PDA was bound to the PAM network through the interactions between the amino as well as catechol groups in PDA and the amino groups in PAM. Magnesium ions (Mg²⁺) was incorporated in the hydrogel for the promoting effects on cell proliferation, differentiation, and tissue regeneration [24–26]. The hybrid crosslinks of covalent bonds and reversible non-covalent bonds in PDA-PAM/Mg²⁺ hydrogel conferred favorable self-healing and adhesive capability. When exposed to NIR irradiation, the PDA in hydrogels displayed excellent photothermal efficiency and antibacterial activities in *E. coli* & *S. aureus*. The photostability and recyclability of photothermal effect were improved by the introduction of Mg²⁺. The cytocompatibility of the composite hydrogel *in vitro* was investigated and the wound healing of the hydrogel dressing was evaluated in a wound infection rat model.

2. Material and methods

2.1. Materials

Acrylamide (AM), ammonium persulfate (APS), *N,N*-methylene bisacrylamide (BIS), magnesium chloride, and tetramethylene ethylenediamine (TMEDA) were purchased from Kelong Chemical Co. (Chengdu, China). Dopamine hydrochloride was purchased from Aladdin Bio-Chem Technology (Shanghai, China). *Staphylococcus aureus* (*S. aureus*, ATCC 6538, Gram-positive) and *Escherichia coli* (*E. coli*, ATCC 8739, Gram-negative) were used for the antibacterial experiments. 3-(4,5-Dimethyl-2-thiazolyl)-2,5-diphenyl tetrazolium bromide (MTT) was obtained from Energy Chemical Technology (Shanghai, China).

2.2. Preparation of hydrogels

Dopamine hydrochloride (12.8 mg) was dissolved in 8 mL PBS aqueous solution (pH 11) and stirred at room temperature for 10 min to

form stable PDA solution, which was then mixed with 1600 mg AM, 160 mg APS, 8 mg BIS, and 9.6 mg magnesium chloride for 5 min. TMEDA was added and the mixture was immediately vortexed to obtain PDA-PAM/Mg²⁺ hydrogel. The PAM-PDA hydrogel was prepared in the absence of magnesium chloride. Similarly, PAM was prepared as a control sample without addition of PDA and Mg²⁺.

2.3. Physicochemical characterization of hydrogels

The attenuated total reflection Fourier transform infrared (FT-IR) spectroscopy of PAM, PAM-PDA, and PDA-PAM/Mg²⁺ hydrogels were measured on an infrared spectrometer (Invenio-R, American), in which the scanning range was set from 400 cm⁻¹ to 4000 cm⁻¹ with a resolution of 4 cm⁻¹. X-ray photoelectron spectroscopy (XPS, Kratos, AXISSupra, UK) was utilized to analyze the chemical composition of PDA-PAM/Mg²⁺ hydrogel. Under the condition of the voltage of 15 kV and the current of 5 mA, the monochromatic Alka X-ray was used as the excitation source ($h\nu = 1486.6$ eV). The micro-morphology of hydrogels was observed by a scanning electron microscope (SEM, S4800, Hitachi Ltd, Japan). Before the examination, all the samples were freeze-dried and sprayed with a thin gold layer. The pore size distribution and the porosity were calculated using the software Image J by measuring the images obtained by SEM. The equilibrated swelling ratios (ESR) of hydrogels were determined by swelling tests. The freeze-dried hydrogel samples with the same volume were immersed into PBS (pH = 7.4) at 37 °C for 24 h until swelling equilibrium. Then the samples were taken out and weighed after the removal of superfluous water. The ESR was calculated according to the formula as:

$$\text{ESR} = (W_s - W_d)/W_d \times 100\%$$

where W_s and W_d represent the weight of the hydrogels at the swollen and the dry states, respectively. The test was repeated three times.

2.4. Self-healing behavior

The self-healing capacity of the hydrogels was evaluated by macroscopic autonomous healing and rheological recovery test. The hydrogel sample with a diameter of 2.5 cm and a height of 0.3 cm was cut into two halves. The cross-sections of the two halves were closely contacted to observe the self-healing behavior. The gel state of the sample was observed after 2 h.

A strain amplitude sweep test of the hydrogel disks was carried out on an Antonpa rheometer (MCR302, Austria) to determine the linear viscoelastic region and the value of critical strain. A freshly prepared hydrogel was tested by an alternate strain sweep test with a strain range from 1% to 10,000% and a constant frequency of 1 Hz.

Amplitude oscillatory strains were switched from small strain (2%)

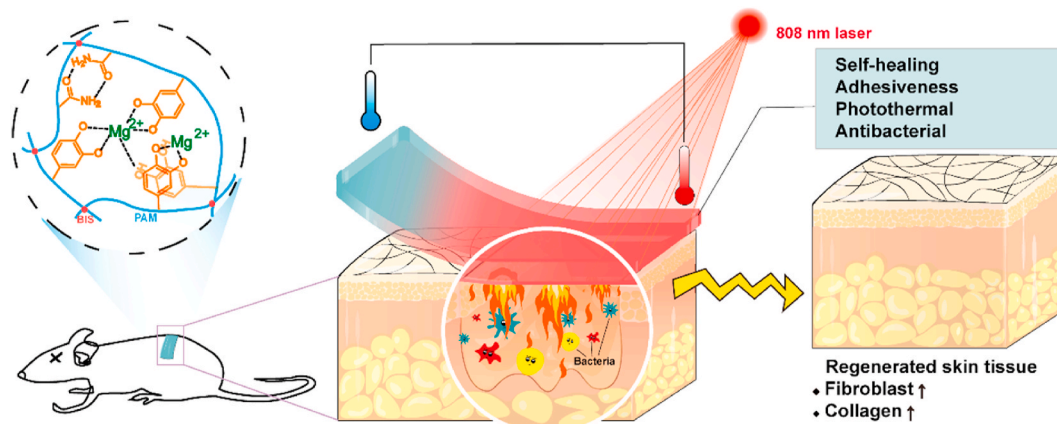


Fig. 1. Schematic illustration for the mechanism and application of PDA-PAM/Mg²⁺ hydrogel in wound healing in a full-thickness defect model.

to large strain (1000%) and 5 cycles were carried out.

2.5. Adhesion property

The adhesion properties of hydrogels were tested by a universal testing machine (Shimadzu, AGS-J, USA) and a macroscopic adhesion test. Various substrates, including porcine skin, polyethylene (PE) film, glass slide, and aluminum (Al) plate, were employed to investigate the adhesive properties through tensile-adhesion testing. The substrates bonded with the hydrogels (20 mm × 20 mm) were compressed for a few minutes at room temperature, and the tensile adhesive strength of the hydrogel was measured at a constant speed of 5 mm/min ($n \geq 5$). Besides, the macroscopic adhesion test of the hydrogels adhered to various substrates was also conducted.

2.6. Photothermal effect

The photothermal conversion of hydrogels was studied by continuously irradiating the materials in a tube filled with 1 mL gel for 10 min by using an 808 nm NIR laser (2 W cm⁻²). Simultaneously, FLIRE 60 infrared thermal imager was employed to monitor the temperature changes and capture thermal images. Photothermal stability was carried out according to our previous study [27].

2.7. Antibacterial activity

The *in vitro* antibacterial activities of hydrogels were investigated by using *S. aureus* and *E. coli* as model bacteria. Gels were co-cultured with bacteria to evaluate the inhibitory effect. Specifically, the prepared hydrogel samples (diameter: 15 mm; thickness: 3 mm) were added into a 48-well plate. Bacteria suspension in Luria-Bertani (LB) medium (1 × 10⁶ CFU mL⁻¹) was added to co-culture with hydrogel. The experiment was divided into four groups ($n = 4$):

- PAM: PAM gel control group and light treatment;
- PAM-PDA: PAM-PDA gel and light treatment;
- PDA-PAM/Mg²⁺: PDA-PAM/Mg²⁺ gel and light treatment;
- and Control group: only medium, no other treatment.

The 48-well plate was exposed to a 660 nm laser (2 W cm⁻²) for 10 min. After that, 30 μL medium of each hole was diluted with 10 mL PBS, then 50 μL dilution was coated on the solid medium. The agar plates were cultured in the incubator for 14 h and then photographed. On the other hand, the 24-well plate was incubated in an incubator for 14 h, and 100 μL medium was taken from each well. The optical density (OD) of medium at 600 nm was measured by a microplate reader (Biorad, USA).

2.8. Cytocompatibility assay

MTT colorimetry and living/dead cell staining were used to explore the effect of materials on cell growth. Mouse embryonic fibroblast cells (NIH/3T3) and fibroblast cells (L929) were cultured in DMEM supplemented with 10% FBS and 1% penicillin-streptomycin in a CO₂ incubator at 37 °C. After cells adhered to the plate for 12 h, the medium was replaced with 200 μL of hydrogel extracts. After incubated for additional 48 h, 20 μL of MTT solution was added into each well and incubated for 4 h. Eventually, the medium was replaced by 200 μL DMSO and analyzed by a microplate reader (Biorad, USA) using an excitation wavelength of 490 nm. The cell viability was calculated according to a previous study [28,29].

Live/dead staining was conducted using NIH/3T3 and L929 cells, which were seeded into a 6-well plate. Briefly, after cells adhered to the plate for 12 h, the cells were incubated with hydrogel extracts for 48 h. Next, cells were stained with Calcein-AM/PI dye for 25 min and observed under a fluorescent microscope (Olympus IX71, Japan) at excitation/emission wavelengths of 530/580 nm and 490/515 nm for PI

and Calcein-AM, respectively. All Experiments were performed in triplicate.

The cell scratch assay was performed after cells adhered to the plate. Cells were incubated with the extracts of hydrogels and imaged using inverted optical microscopy at 0, 24, 48, and 72 h. The scratch area rate was obtained by the equation:

$$\text{Scratch area rate (\%)} = (A_t / A_0) \times 100\%$$

where A_t and A_0 were the scratch areas on day t and day 0, respectively.

2.9. In vivo wound healing evaluation

Animal experiments comply with the National Regulations on the Administration of Laboratory Animals and were approved by the Animal Care and Use Committee of Sichuan University. Sprague Dawley (SD) rats (male, approximately 260 g) were purchased from the Dashuo Biotechnology Co. Ltd. All rats were acclimatized for a week and then the back hair was shaved. Full-thickness wound model was established at the dorsal area of SD rats. Four full-thickness defect wounds with a diameter of 1 cm were symmetrically made on each side of the spine after rats were anesthetized by intraperitoneal injection of 10% chloral hydrate. Thereafter, 100 μL *S. aureus* (10⁸ CFU mL⁻¹) was injected into the wound to establish infection. The wounds of each rat were covered with PAM, PAM-PDA, and PDA-PAM/Mg²⁺ hydrogel, respectively ($n = 5$). The hydrogels were treated with 808 nm NIR laser (2 W cm⁻²) for 10 min. Medical nonwovens were then used to fix wound dressings. During the experiment period, the wound dressings were replaced every three days. The wound sites were photographed on days 0, 3, 7, and 14. Wound areas were measured using the Image J software and wound closure calculated as follows:

$$\text{Wound closure (\%)} = (1 - (A_t / A_0)) \times 100\%$$

where A_t and A_0 were the wound areas on day t and day 0, respectively.

2.10. Histological analysis

After a 14-day treatment, the skin tissues were collected and fixed in 4% paraformaldehyde solution. The tissue was embedded in paraffin and cross-sectioned to 5 μm thick slices. The tissue sections were stained with hematoxylin-eosin (H&E) reagents and Masson [30]. All slices were analyzed and photo-captured on a microscope (Leica, Germany).

2.11. Statistical analysis

Statistical analyses were performed using SPSS 25.0 software for Windows. Data were presented as means ± standard deviation. The difference in the values between the two groups was determined by *t*-test. The statistical significance of more than two groups was assessed using one-way ANOVA. A value of * $p < 0.05$ was considered statistical differences and ** $p < 0.01$ was considered statistically significant differences.

3. Results and discussion

3.1. Preparation and physicochemical characterization of hydrogels

In this study, the composite hydrogels were produced by a two-step procedure. Firstly, polydopamine (PDA) was synthesized by an alkali-induced pre-polymerization. Secondly, the PDA-PAM/Mg²⁺ hydrogel was fabricated by an aqueous radical polymerization. Control hydrogels PAM and PAM-PDA were prepared similarly. FT-IR spectrometry was used to investigate possible crosslinks within the obtained hydrogels. The assignments of infrared light absorption peaks were shown in Fig. 2a and Table 1. Compared with pure PAM hydrogels, the spectra of PAM-PDA and PDA-PAM/Mg²⁺ hydrogels depicted a new peak at 1258

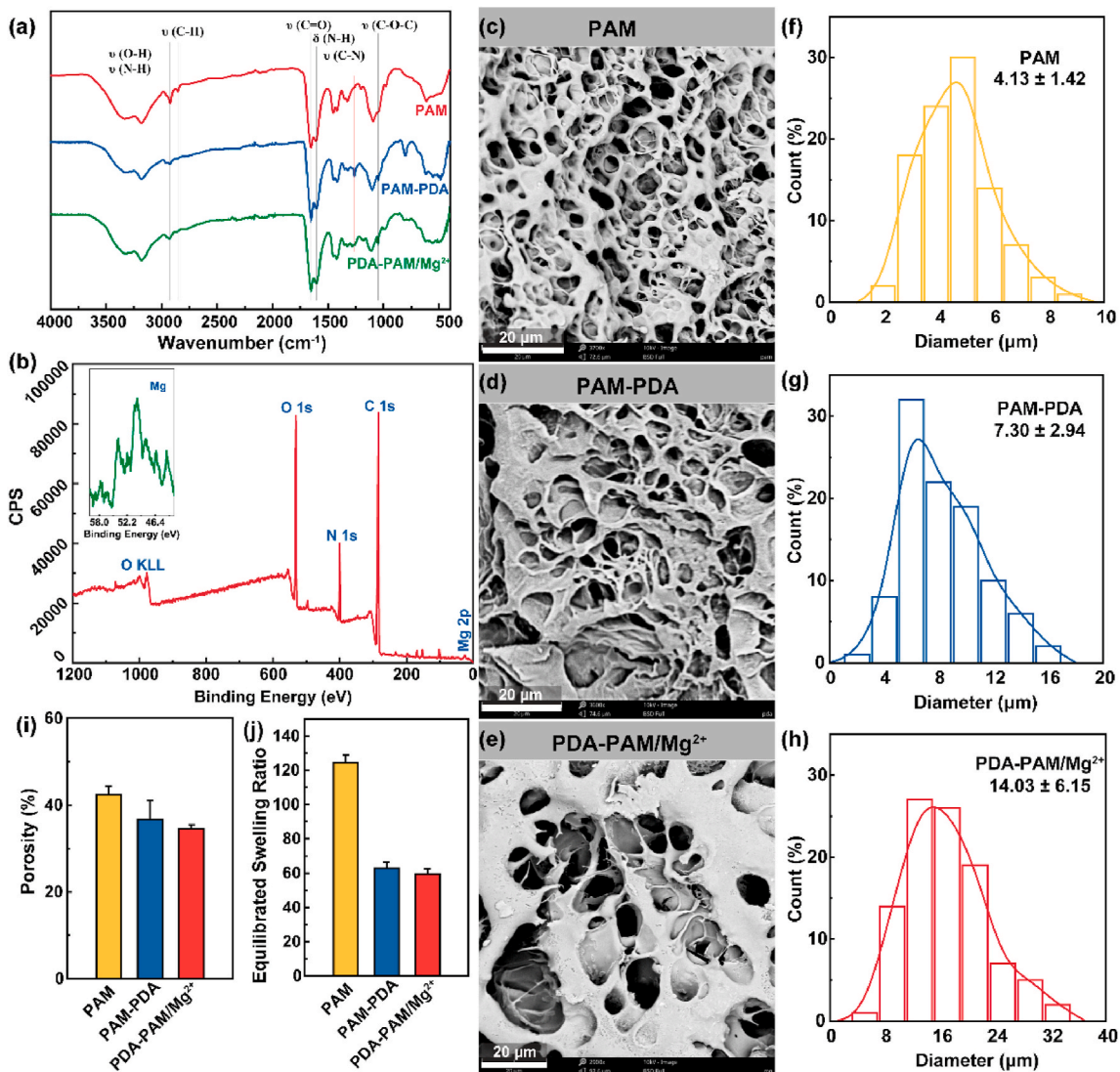


Fig. 2. Characterization of hydrogels. (a) The FTIR spectra of different hydrogels. (b) XPS characterization of PDA-PAM/Mg²⁺ hydrogel. SEM images of PAM (c), PAM-PDA (d), and PDA-PAM/Mg²⁺ (e) hydrogels. The pore size distributions of PAM (f), PAM-PDA (g), and PDA-PAM/Mg²⁺ (h). The porosity (i) and SER (j) of hydrogels.

Table 1
Assignment of FT-IR spectra (Fig. 1a) of hydrogels.

| Number | Wavenumber (cm ⁻¹) | Peak assignments |
|--------|--------------------------------|--------------------------------------------|
| 1 | 3100–3400 | O–H and N–H stretching vibration |
| 2 | 2925 | CH ₂ antisymmetric vibration |
| 3 | 2850 | CH ₂ symmetric vibration |
| 4 | 1650 | C=O stretching vibration for amido |
| 5 | 1600 | N–H bending vibration for primary amide |
| 6 | 1400 | C–N stretching vibration for primary amide |
| 7 | 1450 | CH ₂ in-plane scissoring |
| 8 | 1350 | C–H Bending vibration |
| 9 | 1100 | NH ₂ in-plane rocking |

cm⁻¹, which was corresponding to the C–N stretching vibration. The appearance of new peak presented that there was an interaction between amino groups in PAM and phenolic hydroxyl groups in PDA. Moreover, the wide-scan XPS spectrum of PDA-PAM/Mg²⁺ hydrogel was measured (Fig. 2b), which indicated that the main chemical components of gel included organic elements C, O, and N and inorganic Mg. The XPS result evidenced the successful encapsulation of Mg²⁺ in the hydrogel.

The microstructures of hydrogels were observed by SEM. As

demonstrated in Fig. 2c–e, compared with PAM hydrogel with smooth surfaces, the hydrogels containing PDA had a microfibril structure. The formation of microfibrils in the PAM-PDA and PDA-PAM/Mg²⁺ gels were attributed to the complexation of PDA and PAM chains through π - π interactions and hydrogen bonds [31], which facilitated the broken hydrogel for self-healing. The pore size distributions were obtained from the SEM images and the average diameters of PAM, PAM-PDA, and PDA-PAM/Mg²⁺ hydrogels were 4.13, 7.30, and 14.03 μ m, respectively (Fig. 2f–h). It gradually became larger with the addition of PDA and Mg²⁺, but the porosity of hydrogels containing PDA were smaller than the PAM hydrogel (42.38%), and the smallest value belonged to PDA-PAM/Mg²⁺ hydrogel (34.54%) (Fig. 2i). Consequently, the ESRs of hydrogels containing PDA were lower than the PAM hydrogel (124.52%) (Fig. 2j), which was due to the increased crosslinking density with the addition of PDA and Mg²⁺ in the hydrogel matrix. Even the ESR of PDA-PAM/Mg²⁺ hydrogel was 59.48%, it could swell sharply and absorb tissue surplus exudates, suggesting its potential application in wound dressing.

3.2. Self-healing behavior of the hydrogel

Self-healing hydrogels have promising applications in wound closure by prolonging the service life of hydrogel and preventing wound infection. The self-healing performance of PDA-PAM/Mg²⁺ hydrogel was evaluated by macroscopic observations after cutting the hydrogels in two halves (Fig. 3a). After a 2-h contact, the two halves stuck together to form an intact gel, indicating the natural healing without any external forces. The self-healed hydrogel was well stretched without crack. The self-healing behavior of hydrogels could be explained as the recombination of hydrogen bonds and π - π interactions, which was promoted by the mutual diffusion of free polyacrylamide chains and polydopamine at the incision (Fig. 3b).

The self-healing behavior was also assessed by a rheological recovery test. An amplitude strain sweep test (strain 1–10,000%) was conducted to determine the linear viscoelastic region (LVR) and intersecting point. As illustrated in Fig. 3d, the G' and G'' curves, intersected at a strain of 670%. The higher critical strain indicated that the hydrogel could sustain a larger deformation. Once the strain exceeded the critical strain, the structure of the hydrogel would collapse and converse from a solid with gel properties to a liquid with fluid properties as the G' value decreased dramatically. The self-healing property was further confirmed. As shown in Fig. 3e, when a strain of 1000% was applied, the G' value was lower than G'' value, that indicated that the cross-linking network of hydrogel was destroyed [32]. However, the values recovered ($G' > G''$) when the strain of 1000% returned to 2.0%, clearly demonstrating the reconstruction/self-healing of hydrogel structure. When the two processes were repeated, the reversible rheological

behavior was observed. More importantly, the G' value was recovered to a larger value than the initial G' value when the strain turned low strain. The higher G' value implied a good recovery which was mainly due to the increase of cross-linking points with the rearrangement of polymer molecular chains after the higher strain was applied. This conclusion was further confirmed by the sticky and sandy hydrogel at the end of the experiment, which was remarkably different from the dollop-like PAM (Fig. 3c).

3.3. Stable and strong adhesion capacity of PDA-PAM/Mg²⁺ gel

The adhesive hydrogels that completely adhere and integrate with the tissues could afford a beneficial microenvironment to avoid infections and promote healing. PDA-PAM/Mg²⁺ hydrogel was firmly adhered to an elbow joint even when it adopted different angles (Fig. 4a), suggesting a potential in providing a stable and close contact between the gel and the dynamic wound. The hydrogels also exhibited good adhesion to various material surfaces (hydrophilic, hydrophobic, metallic, and organic tissues) and could bear a heavy load of 100 g (Fig. 4b). Furthermore, the adhesion strength of the hydrogel to representative surfaces was quantified by a tensile-adhesion test (Fig. 4c). The highest adhesion strength to glass, PE, Al, and porcine skin was 41.22, 28.99, 38.58, and 3.69 KPa, respectively (Fig. 4d). The high adhesion of the hydrogel was mainly due to hydrogen bonds formed between amide groups of PAM and functional groups on the surface of various substances. Another key component, polydopamine, could enhance the adhesive force and further improvement of adhesiveness strength. The catechol group formed strong covalent bonds and hydrogen bonds with

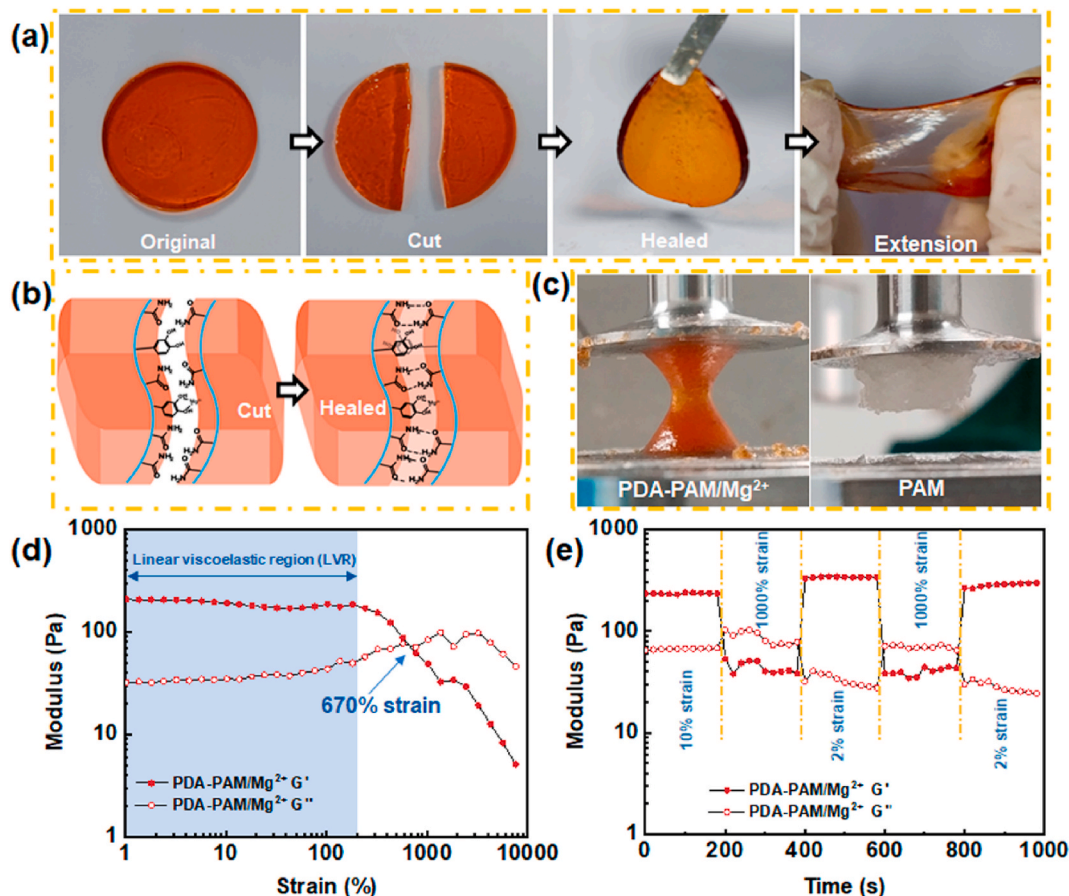


Fig. 3. Self-healing properties of the PDA-PAM/Mg²⁺ hydrogel. (a) Photographs of the self-healing process with disk-shaped hydrogel. (b) Proposed self-healing mechanism of the hydrogel via hydrogen bonds and π - π interactions. (c) The different states of hydrogels at the end of the experiments. (d) Rheological data of the hydrogel from the strain amplitude sweep test (1–10,000%) at 1 Hz frequency. (e) Rheological data of the hydrogel from alternate step strain switching from low strain to high strain.

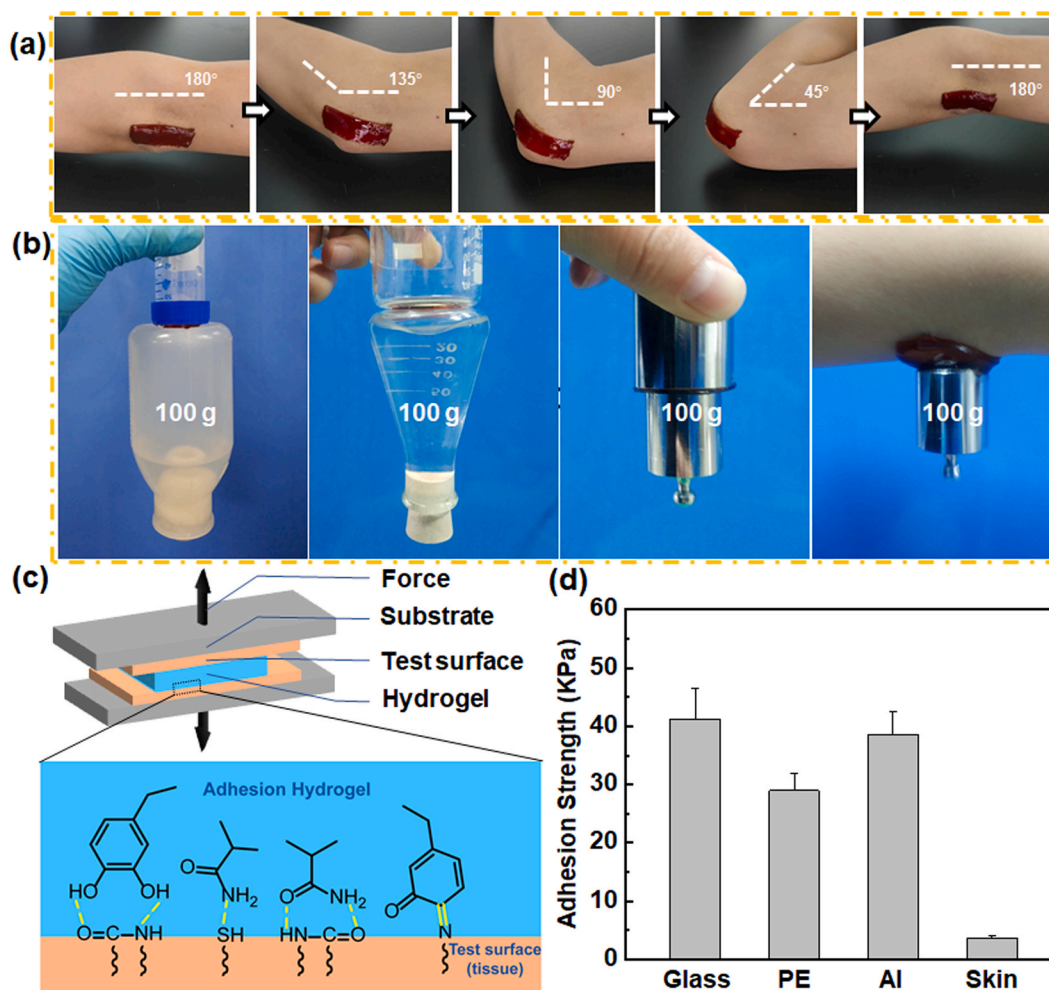


Fig. 4. Adhesive properties of the PDA-PAM/Mg²⁺ hydrogel. (a) Adhesion effect of the hydrogel on human elbow during exercise. (b) Digital images demonstrating the macroscopic adhesion of the hydrogel to various substrates. (c) Schematic illustration of tensile-adhesion testing and adhesion mechanism of hydrogel on tissue. (d) Adhesive strengths of hydrogels on various substrates (glass, PE, Al, and skin).

different nucleophilic reagents (Fig. 4c) [33]. The excellent adhesion property of PDA-PAM/Mg²⁺ gel suggested its potential application in wound dressing by skin protection in a convenient manner.

3.4. Photothermal effect

The photothermal effect could stimulate local microcirculatory blood flow, inhibit bacteria, and reduce inflammation. Thus, the photothermal effects of the hydrogels were studied by irradiating the hydrogel samples under an NIR laser (808 nm, 2 W cm⁻²). Photothermal images and corresponding temperature change curves of different hydrogels were presented in Fig. 5a–d. After irradiation for 10 min, PAM-PDA and PDA-PAM/Mg²⁺ hydrogels showed a temperature increase of 23.0 and 24.8 °C (Fig. 5d), which was significantly higher than that of PAM hydrogel (5.7 °C). These results indicated that PAM hydrogel had no photothermal effect, and PDA containing hydrogels possessed excellent photothermal conversion efficiencies. In addition, the photothermal stability was studied by performing laser on/off experiments in four irradiation-cooling cycles. As shown in Fig. 5e, PDA-PAM/Mg²⁺ showed a higher photothermal stability than PAM-PDA; after four on/off cycles, PAM-PDA can only induce an elevated temperature of 14.3 °C, lower than that of PDA-PAM/Mg²⁺ (21.3 °C). Taking together, the results manifested that the addition of Mg²⁺ could improve the stability and repeatability of photothermal effect.

3.5. Antibacterial performances of PDA-PAM/Mg²⁺

Encouraged by the high photothermal conversion performance, we sought to study the *in vitro* photothermal antibacterial activity of PDA-PAM/Mg²⁺ against *S. aureus* and *E. coli*. After laser treatment, PAM induced an 88.35% survival of *S. aureus* (Fig. 5f), which was significantly higher than those of PAM-PDA (7.72%) and PDA-PAM/Mg²⁺ (5.29%) groups. Similarly, the survival rate of *E. coli* treated with PAM hydrogel was 87.67%, much higher than those of bacteria treated with PAM-PDA (8.09%) and PDA-PAM/Mg²⁺ (7.06%). Owing to Mg²⁺-synergized photothermal antibacterial activity under NIR irradiation, the PDA-PAM/Mg²⁺ hydrogel showed a lower survival rate (<10%) than the previously reported Mg²⁺-based carboxymethyl cellulose (CMC) and silk fibroin (SF) composite hydrogel (CMC/SF/Mg(OH)₂, approximately 20%) [34].

Besides, the antibacterial effects of different hydrogels without light irradiation were studied (Fig. 5g). PAM and PAM-PDA showed very limited antibacterial efficacy; 93.29% of *S. aureus* and 94.31% of *E. coli* were alive after treated with PAM-PDA. In contrast, PDA-PAM/Mg²⁺ showed a significantly enhanced antibacterial activity, resulting into a survival rate of 76.77% for *S. aureus* and 74.82% for *E. coli*. These results were further intuitively verified by the bacterial coating plates (Fig. 5h and i). PDA-PAM/Mg²⁺ showed better antibacterial activity than PAM-PDA owing to the Mg²⁺-mediated antibacterial effect, which was consistent with previous studies [35,36]. Taking together,

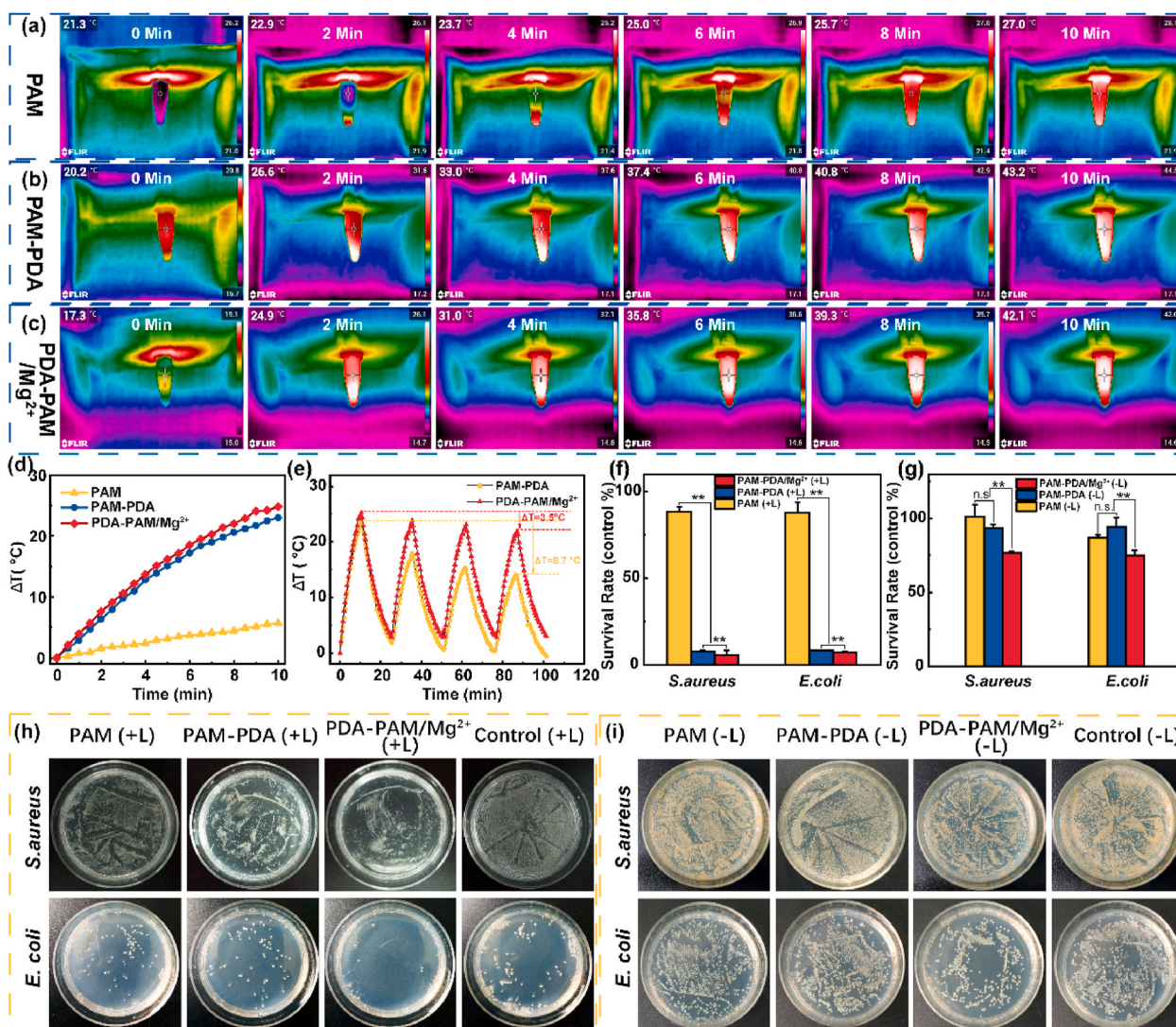


Fig. 5. Photothermal and antibacterial effects of the hydrogels. Infrared photothermal images of the PAM (a), PAM-PDA (b), and PDA-PAM/Mg²⁺ (c) under NIR laser irradiation. (d) Photothermal curves of different hydrogels. (e) Temperature changes of the two hydrogels with repeated NIR irradiations. Survival rates (f, g) and images (h, i) of *S. aureus* and *E. coli* after treatment with different hydrogels in the presence (f, h) and absence (g, i) of NIR irradiation (**p* < 0.05; ***p* < 0.01).

PDA-PAM/Mg²⁺ displayed an improved antibacterial activity via a photothermal and Mg²⁺ synergy.

3.6. Cytocompatibility evaluation of the hydrogels

The cytocompatibility is essential for hydrogel dressings. The cell biocompatibility of the hydrogels was first evaluated by an MTT assay. As shown in Fig. 6b, there was no significant differences in the relative survival rates between NIH/3T3 and L929 cells cultured in all hydrogel extracts, and the viability of cells cultured in all hydrogel extracts was higher than 85% after a 48-h incubation, indicating that the prepared hydrogels have good cytocompatibility [30,37].

Next, a live/dead staining assay was used to visually evaluate the cell biocompatibility. As shown in Fig. 6a, after a 2-d co-culture, most cells were alive and spaced regularly with spindle-like morphology and only a few cells were dead, revealing that the hydrogels nearly had no cytotoxicity. Therefore, live/dead staining and MTT results manifested that PAM, PAM-PDA, and PDA-PAM/Mg²⁺ hydrogels were cytocompatible and could be used for tissue repair.

Furthermore, a cell scratch assay was performed to explore the impacts of hydrogels on the migration, motility, and proliferation of cells. The results were shown in Fig. 6c, the scratch area decreased in all

hydrogel groups over time, especially in PDA-PAM/Mg²⁺ group. The semi-quantitative analysis of scratch area revealed that there was PDA-PAM/Mg²⁺ group (29.89%) showed a much smaller residual scratch area than PAM (44.57%) and PAM-PDA (43.36%) groups (Fig. 6d), implying that the existence of Mg²⁺ contributed to the enhanced cell migration and proliferation [25,38].

3.7. Evaluation of wound healing and antibacterial activity in vivo of the hydrogels

The wound healing effects of the hydrogels were evaluated by a rat skin full-thickness defect model. Hydrogel dressings were replaced every 3 days. Representative pictures of the wounds in different groups at scheduled time intervals were shown in Fig. 7a. Macroscopically, PDA-PAM/Mg²⁺ hydrogel showed a much higher wound healing efficacy than the other two groups, and no obvious wounds were observed in the PDA-PAM/Mg²⁺ group after a 14-day treatment. Furthermore, the quantitative wound areas and wound closure were calculated based on the wound photographs (Fig. 7b). After treatment for 3 days, PAM, PAM-PDA, and PDA-PAM/Mg²⁺ hydrogel groups displayed wound closure of 13.12%, 14.31%, and 18.06%, respectively. On day 7, the wound closure in PDA-PAM/Mg²⁺ hydrogel group was 79.46%, much larger

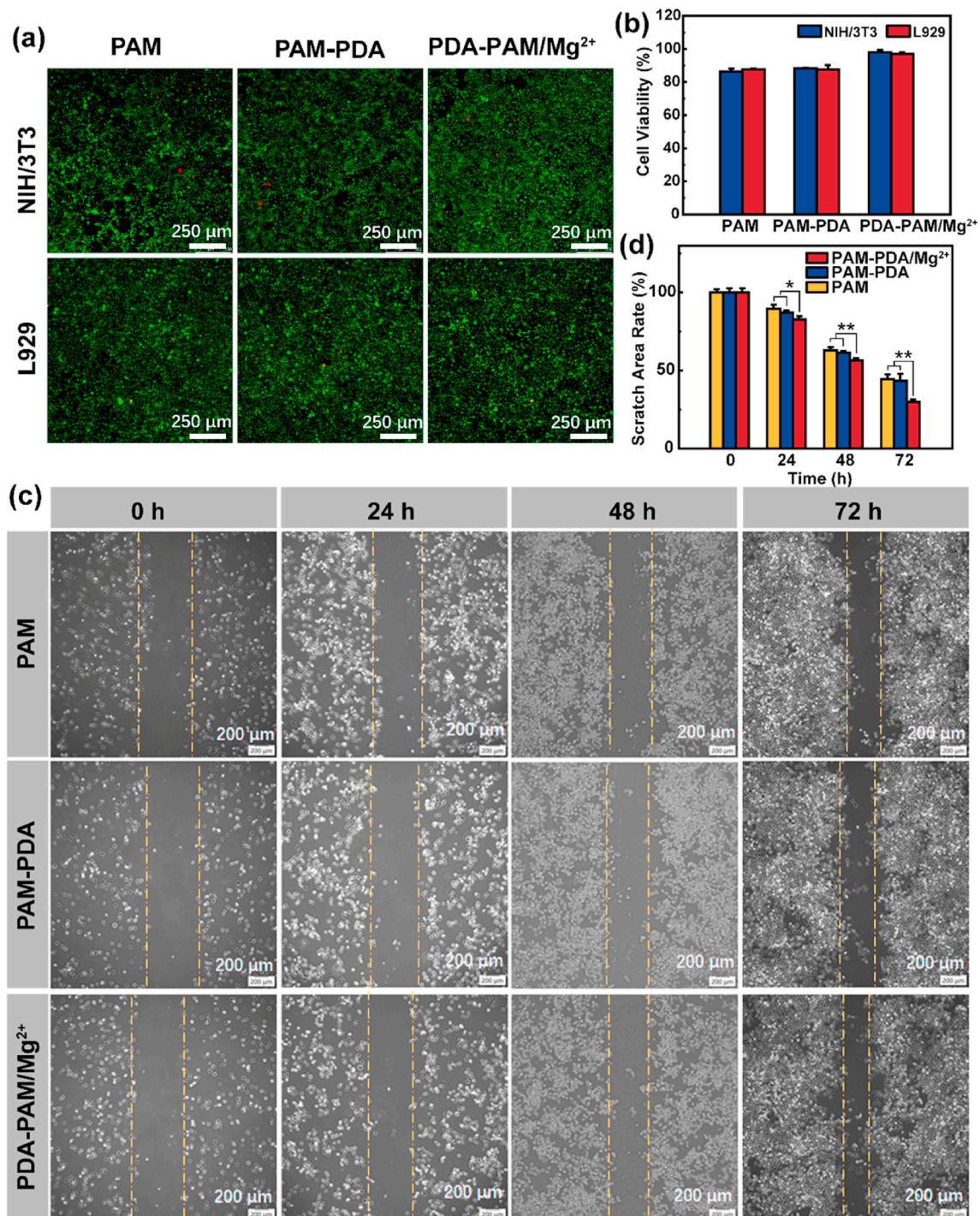


Fig. 6. Cytocompatibility of the hydrogels. Live/dead staining (a) and cell viability (b) of NIH/3T3 and L929 cells after treated with hydrogels for 2 d. (c) Representative images of the scratch area of L929 cells at different time points. (d) Quantitative analysis of the relative scratch area of L929 cells at different time points (* $p < 0.05$, ** $p < 0.01$).

than that of PAM (62.01%) and PAM-PDA (65.50%). On the 14th day, all wounds in PDA-PAM/Mg²⁺ group were completely cured, verifying a much better wound healing effects than PAM and PAM-PDA. Together, these results clearly demonstrated that the desirable physicochemical characteristics endowed the PDA-PAM/Mg²⁺ hydrogel the best wound healing efficiency. Compared with another Mg²⁺-based hydrogel (21 days) composing of PAM and Gellan Gum (GG), our PDA-PAM/Mg²⁺ gel (14 days) still showed a shorter healing time [39].

The *in vivo* antibacterial efficacy of hydrogels was evaluated by collecting skin tissues of the wound sites and bacteria on the them with

swabs after the treatment with hydrogels for 24 h. On the one hand, the survived bacteria on the wound sites were checked through Gram-staining; on the other hand, the collected bacteria were incubated in a 37 °C incubator for 4 h. Then the optical density (OD) of the medium of bacteria at 600 nm was measured and the medium diluted with PBS for the bacterial coating experiment. The results were shown in Fig. 8a and b, both the Gram-staining of the skin tissue sections and the colony study suggested that PAM-PDA and PDA-PAM/Mg²⁺ plus laser treatment induced significant elimination of *S. aureus*. This result was confirmed by the quantitative analysis of *S. aureus*, where OD value of PAM group

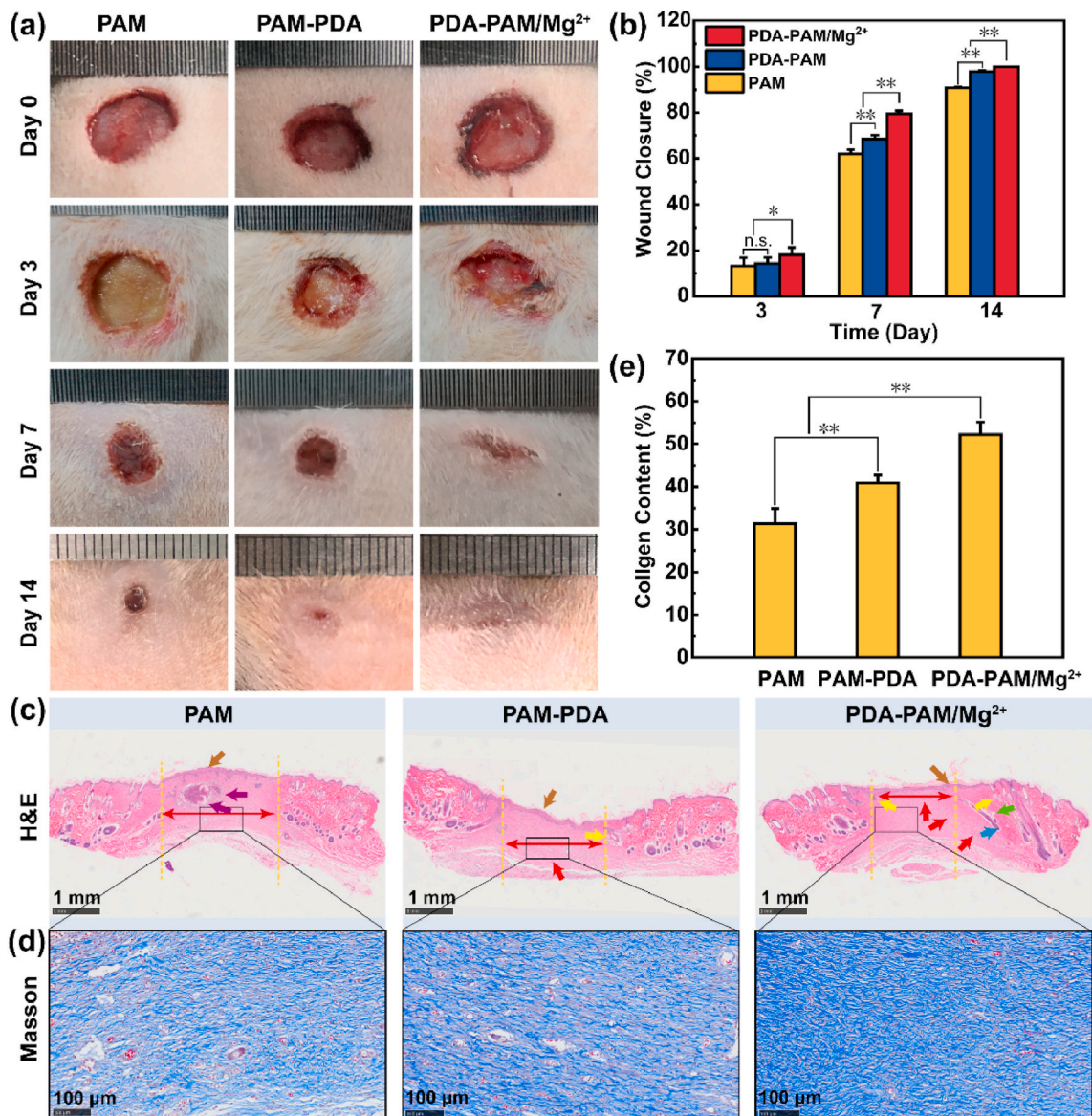


Fig. 7. Wound healing effects *in vivo* of the hydrogels. (a) Images of the wounds in rats following treatment with different hydrogels onto the wound area after surgical removal. (b) The wound closure at the indicated time points for each group. (c) H&E-stained histological images of the wound tissues from each treatment group (brown, red, blue, green, yellow, purple arrows represent epithelium, vessels, hair follicles, sebaceous gland, sweat glands, inflammatory cells, respectively). (d) Masson staining histological images of the regeneration of skin tissue after treated for 14 days. (e) Quantitative analysis of collagen content (%) in the different treatment groups based on Masson staining. (* $p < 0.05$; ** $p < 0.01$).

(0.13) is much larger than those of PAM-PDA (0.074) and PDA-PAM/Mg²⁺ (0.056) (Fig. 8c). Overall, PDA-PAM/Mg²⁺ group showed the best antibacterial effect, which consistent with the *in vitro* antibacterial results.

3.8. Histological analysis

Histological analysis was carried out to further evaluate the wound healing effect of hydrogel dressings. H&E staining results of the regenerated skin tissues that were collected on day 14 were shown in Fig. 7c. All hydrogel groups exhibited a regenerated epithelium layer (brown arrows). Fewer inflammatory cells were observed in the PAM-PDA and PDA-PAM/Mg²⁺ groups, which was attributed to the photothermal elimination of *S. aureus*. More granulation tissues were replaced with the migration of fibroblasts to the wound site (red double-headed arrows), which was mainly due to the presence of Mg²⁺. Moreover, some hair follicles, sweat glands, and sebaceous glands were observed in the PDA-

PAM/Mg²⁺ group. These results suggested that the PDA-PAM/Mg²⁺ displayed the most promising wound healing effects amongst all hydrogels.

Collagen deposition plays an important role in scar contraction, re-epithelialization and preliminary dermis construction [40,41]. The collagen deposition in the treated skins was evaluated by Masson staining (Fig. 7d). After 14 days of treatment, the collagen fibers of the skin tissues treated with PDA-PAM/Mg²⁺ were thicker, denser, and better arranged. The collagen content in PDA-PAM/Mg²⁺ group (52.2%) was significantly higher than PAM (31.4%) and PAM-PDA (40.8%) groups (Fig. 7e), confirming the better tissue repairing property.

4. Conclusion

In this work, a multi-functional PDA-PAM/Mg²⁺ hydrogel was reported for wound treatment. With strong supramolecular interactions existing in the hydrogel, including hydrogen bonding, coordination

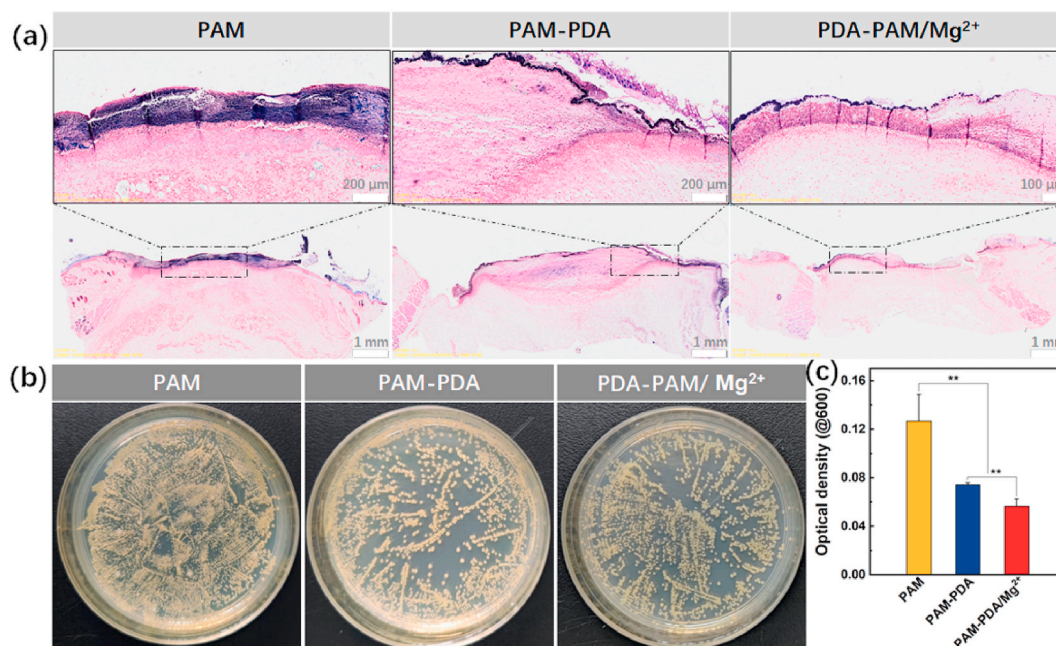


Fig. 8. The *in vivo* antibacterial performances of hydrogels. (a) The Gram-staining images of the rat skin tissues infected with *S. aureus* after different hydrogel treatments. (b) The photographs of representative colonies of *S. aureus* upon treatments. (c) The optical density of *S. aureus* after collection from wounds and a 4-h proliferation. (***p* < 0.01).

effect, and π - π stacking interactions, the prepared hydrogel exhibited excellent self-healing and adhesiveness properties. The introduction of PDA endowed the gel with outstanding photothermal effect. More importantly, the hydrogel inherited excellent thermal stability with the presence of Mg^{2+} . Benefiting from PTT, hydrogels containing PDA possessed a good antibacterial effect on *E. coli* and *S. aureus*. Moreover, the PDA-PAM/ Mg^{2+} hydrogel had good cytocompatibility and possessed wound restoration in effective accelerating way as proved by full-thickness skin defect repair experiments. In summary, multifunctional PDA-PAM/ Mg^{2+} hydrogel is a bacteriostatic wound dressing for accelerating wound healing and holds a potential in future clinical adjuvant treatment.

CRedit authorship contribution statement

Zhaoyuan Guo: Methodology, Investigation, Data curation, Writing – original draft, preparation. **Zhuangzhuang Zhang:** Methodology, Software, Formal analysis. **Nan Zhang:** Software, Formal analysis. **Wenxia Gao:** Conceptualization, Formal analysis. **Jing Li:** Visualization, Formal analysis. **Yuji Pu:** Conceptualization, Supervision, Funding acquisition. **Bin He:** Writing – review & editing, Funding acquisition, Supervision, Project administration. **Jing Xie:** Conceptualization, Project administration, Resources.

Declaration of competing interest

The authors declare that they have no known competing financial interests or personal relationships that could have appeared to influence the work reported in this paper.

Acknowledgement

This work was supported by the National Natural Science Foundation of China (No. 51773130, 52073216 and 51903172). National Science Foundation of Zhejiang province (LY20B040004). The authors would like to thank the Analytical & Testing Center of Sichuan University for FT-IR and XPS tests.

References

- [1] M. Zheng, X. Wang, O. Yue, M. Hou, H. Zhang, S. Beyer, A.M. Blocki, Q. Wang, G. Gong, X. Liu, J. Guo, Skin-inspired gelatin-based flexible bio-electronic hydrogel for wound healing promotion and motion sensing, *Biomaterials* 276 (2021), 121026, <https://doi.org/10.1016/j.biomaterials.2021.121026>.
- [2] Y.-K. Wu, N.-C. Cheng, C.-M. Cheng, Biofilms in chronic wounds: pathogenesis and diagnosis, *Trends Biotechnol.* 37 (5) (2019) 505–517, <https://doi.org/10.1016/j.tibtech.2018.10.011>.
- [3] Y. Yuan, S. Shen, D. Fan, A physicochemical double cross-linked multifunctional hydrogel for dynamic burn wound healing: shape adaptability, injectable self-healing property and enhanced adhesion, *Biomaterials* 276 (2021), 120838, <https://doi.org/10.1016/j.biomaterials.2021.120838>.
- [4] Y. Xu, X. Liu, Y. Zheng, C. Li, K.W. Kwok Yeung, Z. Cui, Y. Liang, Z. Li, S. Zhu, S. Wu, Ag₃PO₄ decorated black urchin-like defective TiO₂ for rapid and long-term bacteria-killing under visible light, *Bioact. Mater.* 6 (6) (2021) 1575–1587, <https://doi.org/10.1016/j.bioactmat.2020.11.013>.
- [5] Y. Tian, Y. Li, J. Liu, Y. Lin, J. Jiao, B. Chen, W. Wang, S. Wu, C. Li, Photothermal therapy with regulated Nrf2/NF- κ B signaling pathway for treating bacteria-induced periodontitis, *Bioact. Mater.* (2021), <https://doi.org/10.1016/j.bioactmat.2021.07.033>.
- [6] X. Zhang, G. Zhang, H. Zhang, X. Liu, J. Shi, H. Shi, X. Yao, P.K. Chu, X. Zhang, A bifunctional hydrogel incorporated with CuS@MoS₂ microspheres for disinfection and improved wound healing, *Chem. Eng. J.* 382 (2020), 122849, <https://doi.org/10.1016/j.cej.2019.122849>.
- [7] X. Wang, Q. Shi, Z. Zha, D. Zhu, L. Zheng, L. Shi, X. Wei, L. Lian, K. Wu, L. Cheng, Copper single-atom catalysts with photothermal performance and enhanced nanozyme activity for bacteria-infected wound therapy, *Bioact. Mater.* 6 (12) (2021) 4389–4401, <https://doi.org/10.1016/j.bioactmat.2021.04.024>.
- [8] X. Zhi, Y. Liu, L. Lin, M. Yang, L. Zhang, L. Zhang, Y. Liu, G. Alfranca, L. Ma, Q. Zhang, H. Fu, J. Conde, X. Ding, D. Chen, J. Ni, J. Song, D. Cui, Oral pH sensitive GNS@ab nanopores for targeted therapy of *Helicobacter pylori* without disturbance gut microbiome, *Nanomed. Nanotechnol. Biol. Med.* 20 (2019), 102019, <https://doi.org/10.1016/j.nano.2019.102019>.
- [9] Z. Yu, L. Jiang, R. Liu, W. Zhao, Z. Yang, J. Zhang, S. Jin, Versatile self-assembled MXene-Au nanocomposites for SERS detection of bacteria, antibacterial and photothermal sterilization, *Chem. Eng. J.* 426 (2021), 131914, <https://doi.org/10.1016/j.cej.2021.131914>.
- [10] E. Ye, M.D. Regulacio, M.S. Bharathi, H. Pan, M. Lin, M. Bosman, K.Y. Win, H. Ramanarayan, S.-Y. Zhang, X.-J. Loh, Y.-W. Zhang, M.-Y. Han, An experimental and theoretical investigation of the anisotropic branching in gold nanocrosses, *Nanoscale* 8 (1) (2016) 543–552, <https://doi.org/10.1039/C5NR07182H>.
- [11] D. He, T. Yang, W. Qian, C. Qi, L. Mao, X. Yu, H. Zhu, G. Luo, J. Deng, Combined photothermal and antibiotic therapy for bacterial infection via acidity-sensitive nanocarriers with enhanced antimicrobial performance, *Appl. Mater. Today* 12 (2018) 415–429, <https://doi.org/10.1016/j.apmt.2018.07.006>.
- [12] K. Ma, Y. Li, Z. Wang, Y. Chen, X. Zhang, C. Chen, H. Yu, J. Huang, Z. Yang, X. Wang, Z. Wang, Core-shell gold Nanorod@Layered double hydroxide nanomaterial with highly efficient photothermal conversion and its application in

- antibacterial and tumor therapy, *ACS Appl. Mater. Interfaces* 11 (33) (2019) 29630–29640, <https://doi.org/10.1021/acsami.9b10373>.
- [13] T. Deng, H. Zhao, M. Shi, Y. Qiu, S. Jiang, X. Yang, Y. Zhao, Y. Zhang, Photoactivated trifunctional platinum nanobiotics for precise synergism of multiple antibacterial modes, *Small* 15 (46) (2019), 1902647, <https://doi.org/10.1002/smll.201902647>.
- [14] L. Feng, C. Zhu, H. Yuan, L. Liu, F. Lv, S. Wang, Conjugated polymer nanoparticles: preparation, properties, functionalization and biological applications, *Chem. Soc. Rev.* 42 (16) (2013) 6620–6633, <https://doi.org/10.1039/C3CS60036J>.
- [15] J. Koehler, F.P. Brandl, A.M. Goepferich, Hydrogel wound dressings for bioactive treatment of acute and chronic wounds, *Eur. Polym. J.* 100 (2018) 1–11, <https://doi.org/10.1016/j.eurpolymj.2017.12.046>.
- [16] Y. Yang, Y. Liang, J. Chen, X. Duan, B. Guo, Mussel-inspired adhesive antioxidant antibacterial hemostatic composite hydrogel wound dressing via photopolymerization for infected skin wound healing, *Bioact. Mater.* 8 (2022) 341–354, <https://doi.org/10.1016/j.bioactmat.2021.06.014>.
- [17] Y. Xiao, L.A. Reis, N. Feric, E.J. Knee, J. Gu, S. Cao, C. Laschinger, C. Londono, J. Antolovich, A.P. McGuigan, M. Radisic, Diabetic wound regeneration using peptide-modified hydrogels to target re-epithelialization, *Proc. Natl. Acad. Sci. U.S.A.* 113 (40) (2016) E5792, <https://doi.org/10.1073/pnas.1612277113>.
- [18] X. Zhang, Y. Li, D. He, Z. Ma, K. Liu, K. Xue, H. Li, An effective strategy for preparing macroporous and self-healing bioactive hydrogels for cell delivery and wound healing, *Chem. Eng. J.* 425 (2021), 130677, <https://doi.org/10.1016/j.cej.2021.130677>.
- [19] Z. Ling, J. Deng, Z. Zhang, H. Sui, W. Shi, B. Yuan, H. Lin, X. Yang, J. Cao, X. Zhu, X. Zhang, Spatiotemporal manipulation of L-arginine release from bioactive hydrogels initiates rapid skin wound healing accompanied with repressed scar formation, *Appl. Mater. Today* 24 (2021), 101116, <https://doi.org/10.1016/j.apmt.2021.101116>.
- [20] Y. Li, R. Fu, Z. Duan, C. Zhu, D. Fan, Construction of multifunctional hydrogel based on the tannic acid-metal coating decorated MoS₂ dual nanozyme for bacteria-infected wound healing, *Bioact. Mater.* (2021), <https://doi.org/10.1016/j.bioactmat.2021.07.023>.
- [21] E.Y. Jeon, B.H. Hwang, Y.J. Yang, B.J. Kim, B.-H. Choi, G.Y. Jung, H.J. Cha, Rapidly light-activated surgical protein glue inspired by mussel adhesion and insect structural crosslinking, *Biomaterials* 67 (2015) 11–19, <https://doi.org/10.1016/j.biomaterials.2015.07.014>.
- [22] M. Mehdizadeh, J. Yang, Design strategies and applications of tissue bioadhesives, *Macromol. Biosci.* 13 (3) (2013) 271–288, <https://doi.org/10.1002/mabi.201200332>.
- [23] Y. Yang, X. Zhao, J. Yu, X. Chen, R. Wang, M. Zhang, Q. Zhang, Y. Zhang, S. Wang, Y. Cheng, Bioactive skin-mimicking hydrogel band-aids for diabetic wound healing and infectious skin incision treatment, *Bioact. Mater.* 6 (11) (2021) 3962–3975, <https://doi.org/10.1016/j.bioactmat.2021.04.007>.
- [24] U. Adhikari, X. An, N. Rijal, T. Hopkins, S. Khanal, T. Chavez, R. Tatu, J. Sankar, K. J. Little, D.B. Hom, N. Bhattarai, S.K. Pixley, Embedding magnesium metallic particles in polycaprolactone nanofiber mesh improves applicability for biomedical applications, *Acta Biomater.* 98 (2019) 215–234, <https://doi.org/10.1016/j.actbio.2019.04.061>.
- [25] J. Xia, H. Chen, J. Yan, H. Wu, H. Wang, J. Guo, X. Zhang, S. Zhang, C. Zhao, Y. Chen, High-purity magnesium staples suppress inflammatory response in rectal anastomoses, *ACS Appl. Mater. Interfaces* 9 (11) (2017) 9506–9515, <https://doi.org/10.1021/acsami.7b00813>.
- [26] M. Yin, J. Wu, M. Deng, P. Wang, G. Ji, M. Wang, C. Zhou, N.T. Blum, W. Zhang, H. Shi, N. Jia, X. Wang, P. Huang, Multifunctional magnesium organic framework-based microneedle patch for accelerating diabetic wound healing, *ACS Nano* (2021), <https://doi.org/10.1021/acsnano.1c06036>.
- [27] Q. Pan, X. Peng, J.-E. Cun, J. Li, Y. Pu, B. He, In-situ drug generation and controllable loading: rational design of copper-based nanosystems for chemothermal cancer therapy, *Chem. Eng. J.* 409 (2021), 128222, <https://doi.org/10.1016/j.cej.2020.128222>.
- [28] X. Peng, Q. Pan, J. Li, W. Zhu, N. Zhang, Y. Pu, K. Luo, B. He, Polymer-directed supramolecular assembly of photosensitizers: evocation of photothermal effect and highly efficient loading of disulfiram for chemo-phototherapy of cancer, *Appl. Mater. Today* 22 (2021), 100931, <https://doi.org/10.1016/j.apmt.2020.100931>.
- [29] Z. Guo, Y. Bai, Z. Zhang, H. Mei, J. Li, Y. Pu, N. Zhao, W. Gao, F. Wu, B. He, J. Xie, Thermosensitive polymer hydrogel as a physical shield on colonic mucosa for colitis treatment, *J. Mater. Chem. B* 9 (18) (2021) 3874–3884, <https://doi.org/10.1039/D1TB00499A>.
- [30] H. Xia, Y. Liang, K. Chen, C. Guo, M. Wang, J. Cao, S. Han, Q. Ma, Y. Sun, B. He, Reduction-sensitive polymeric micelles as amplifying oxidative stress vehicles for enhanced antitumor therapy, *Colloids Surf., B* 203 (2021), 111733, <https://doi.org/10.1016/j.colsurfb.2021.111733>.
- [31] L. Han, L. Yan, K. Wang, L. Fang, H. Zhang, Y. Tang, Y. Ding, L.-T. Weng, J. Xu, J. Weng, Y. Liu, F. Ren, X. Lu, Tough, self-healable and tissue-adhesive hydrogel with tunable multifunctionality, *NPG Asia Mater.* 9 (4) (2017) e372, <https://doi.org/10.1038/am.2017.33>.
- [32] J. Qu, X. Zhao, Y. Liang, T. Zhang, P.X. Ma, B. Guo, Antibacterial adhesive injectable hydrogels with rapid self-healing, extensibility and compressibility as wound dressing for joints skin wound healing, *Biomaterials* 183 (2018) 185–199, <https://doi.org/10.1016/j.biomaterials.2018.08.044>.
- [33] L. Wang, X. Zhang, K. Yang, Y.V. Fu, T. Xu, S. Li, D. Zhang, L.-N. Wang, C.-S. Lee, A novel double-crosslinking-double-network design for injectable hydrogels with enhanced tissue adhesion and antibacterial capability for wound treatment, *Adv. Funct. Mater.* 30 (1) (2020), 1904156, <https://doi.org/10.1002/adfm.201904156>.
- [34] R. Eivazzadeh-Keihan, F. Khalili, N. Khosropour, H.A.M. Aliabadi, F. Radinekiyan, S. Sukhtezari, A. Maleki, H. Madanchi, M.R. Hamblin, M. Mahdavi, S.M. A. Haramshahi, A.E. Shalan, S. Lanceros-Méndez, Hybrid bionanocomposite containing magnesium hydroxide nanoparticles embedded in a carboxymethyl cellulose hydrogel plus silk fibroin as a scaffold for wound dressing applications, *ACS Appl. Mater. Interfaces* 13 (29) (2021) 33840–33849, <https://doi.org/10.1021/acsami.1c07285>.
- [35] N.C. Andrés, J.M. Sieben, M. Baldini, C.H. Rodríguez, Á. Famiglietti, P.V. Messina, Electroactive Mg²⁺-hydroxyapatite nanostructured networks against drug-resistant bone infection strains, *ACS Appl. Mater. Interfaces* 10 (23) (2018) 19534–19544, <https://doi.org/10.1021/acsami.8b06055>.
- [36] R.K. Singh, S. Kannan, Synthesis, Structural analysis, Mechanical, antibacterial and Hemolytic activity of Mg²⁺ and Cu²⁺ co-substitutions in β-Ca₃(PO₄)₂, *Mater. Sci. Eng. C* 45 (2014) 530–538, <https://doi.org/10.1016/j.msec.2014.10.017>.
- [37] Y. Sun, Y. Liang, N. Hao, X. Fu, B. He, S. Han, J. Cao, Q. Ma, W. Xu, Y. Sun, Novel polymeric micelles as enzyme-sensitive nuclear-targeted dual-functional drug delivery vehicles for enhanced 9-nitro-20(S)-camptothecin delivery and antitumor efficacy, *Nanoscale* 12 (9) (2020) 5380–5396, <https://doi.org/10.1039/C9NR10574C>.
- [38] S. Yoshizawa, A. Brown, A. Barchowsky, C. Sfeir, Magnesium ion stimulation of bone marrow stromal cells enhances osteogenic activity, simulating the effect of magnesium alloy degradation, *Acta Biomater.* 10 (6) (2014) 2834–2842, <https://doi.org/10.1016/j.actbio.2014.02.002>.
- [39] W. Li, X. Jian, Y. Zou, L. Wu, H. Huang, H. Li, D. Hu, B. Yu, The fabrication of a Gellan gum-based hydrogel loaded with magnesium ions for the synergistic promotion of skin wound healing, *Front. Bioeng. Biotechnol.* 9 (2021) 709679, <https://doi.org/10.3389/fbioe.2021.709679>.
- [40] H.D. Zomer, T.d.S. Jeremias, B. Ratner, A.G. Trentin, Mesenchymal stromal cells from dermal and adipose tissues induce macrophage polarization to a pro-repair phenotype and improve skin wound healing, *Cytotherapy* 22 (5) (2020) 247–260, <https://doi.org/10.1016/j.jcyt.2020.02.003>.
- [41] T.J. Keane, C.-M. Horejs, M.M. Stevens, Scarring vs. functional healing: matrix-based strategies to regulate tissue repair, *Adv. Drug Deliv. Rev.* 129 (2018) 407–419, <https://doi.org/10.1016/j.addr.2018.02.002>.